Chi Ding[1]
Department of Mechanical and Aerospace Engineering,
Clarkson University,
Potsdam, NY 13699
e-mail: chid@clarkson.edu

Bin Zhang[1]
Department of Mechanical and Aerospace Engineering,
Clarkson University,
Potsdam, NY 13699
e-mail: bzhang@clarkson.edu

Chunlei Liang
Department of Mechanical and Aerospace Engineering,
Clarkson University,
Potsdam, NY 13699

Kenneth Visser
Department of Mechanical and Aerospace Engineering,
Clarkson University,
Potsdam, NY 13699

Guangming Yao
Department of Mathematics,
Clarkson University,
Potsdam, NY 13699

High-Order Large Eddy Simulations of a Wind Turbine in Ducted and Open-Rotor Configurations

High-order large eddy simulations are performed to study the performance and flow fields of a ducted wind turbine (DWT) operating at different tip speed ratios. To evaluate the effects of the duct, simulations with the same tip speed ratios are also performed on the corresponding open-rotor turbine. It is found that the ducted turbine consistently obtains higher power outputs than the open-rotor counterpart, and the duct itself enhances flow turbulence and blade trailing-edge vortices but weakens tip and hub vortices. Flow bifurcation is observed at the largest tip speed ratio and is identified to be caused by blade blockage effects. Comparative simulations are also performed on both turbines under different yaw angles. It is noticed that the ducted configuration is insensitive to small yaw angles and maintains higher power outputs than the open-rotor configuration at all yaw angles. Moreover, it is observed that the wakes of both configurations recover more quickly as the yaw angle increases. [DOI: 10.1115/1.4055989]

1 Introduction

Wind power is an important energy source and has a long history of being exploited [1]. In the 1970s, the interest in developing wind power was boosted by the oil crisis. At that time, a lot of state-funded projects were launched to develop wind power. In 1973, the U.S. government approved about $200 million to support studies on wind turbines [2]. Between 1975 and 1987, the MOD series of wind turbines were erected in the U.S. [3]. During the same period, Denmark built two large experimental turbines in the vicinity of Aalborg [2]. In Sweden, two large wind turbines: WTS-75 and WTS-3, were installed in cooperation with a German company and a U.S. company, respectively [2].

One major design task is to extract more energy from wind via, for example, increasing its blade size. However, the increasing size leads to larger aerodynamic loads and makes turbine blades more vulnerable to aeroelastic issues like flutters [4]. In addition, large wind turbines are more difficult to install in urban areas than small ones [5]. Another solution to improve turbine efficiency is to place the rotor into a diffuser, called a ducted wind turbine (DWT) or a diffuser augmented wind turbine. By doing so, the mass flowrate across the rotor plane increases, producing more power output [6]. The DWT design avoids the problems caused by increasing blade size and is more suitable for installation in urban areas. DWTs have even more advantages, including insensitivity to yawed flow and less tip loss [6]. Therefore, DWTs are a promising way to efficiently harvest wind energy.

To study the performance of DWTs, a lot of theoretical and experimental research have been carried out. In 1956, Lilley and Rainbird [7] performed a one-dimensional theoretical analysis on DWTs. They concluded that adding a duct could improve the power performance, and higher power outputs can be achieved via larger duct expansion ratios. However, a large expansion ratio may cause boundary-layer separation. During the 1970s and 1980s, a series of experiments verified the concept of DWT. Some experiments employing techniques like ring-shaped flaps and multislotted diffusers were also performed to prevent flow separations [8–10].

Many computational studies on DWTs have also been reported. In 1981, Fletcher [11] analyzed a DWT using the blade element momentum theory, which took into account the effects of Reynolds number and wake rotation. Good agreement with experimental measures was achieved. Vaz and Wood [12] improved this blade element momentum method by including a high rotor thrust correction and a new formulation for the far-wake velocity. Koras and Georgalas [13] modeled the rotor of a DWT by a lifting line and the duct by a combination of vortex rings and source rings. They used this potential flow method to study the influence of several geometrical parameters on the power output. However, their method was limited to DWTs with large tip clearance. Politis and Koras [14] later made progress by using a lifting-surface approach for duct modeling, and their method was able to handle DWTs with any tip clearance.

The rapid development of computational fluid dynamics (CFDs) technologies has also boosted the computational studies on DWTs. One of the most popular approaches is to combine a CFD solver with an actuator-disk (AD) model that represents a rotor to study DWTs. This approach is usually referred to as the CFD-AD approach and can provide more details of a DWT flow field at low computational costs. Phillips et al. [15] applied a CFD-AD approach to investigate the Vortec 7 turbine—a full-scale DWT design. In the same way, Hansen et al. [16] analyzed the performance of a DWT and verified that adding a duct increases the mass flowrate. Abe and Ohya [17] employed a CFD-AD approach to study a turbine with a flanged diffuser. Their focus was on how the loading coefficient and the diffuser's

[1]Corresponding authors.

Contributed by the Fluids Engineering Division of ASME for publication in the Journal of Fluids Engineering. Manuscript received May 30, 2022; final manuscript received October 9, 2022; published online November 1, 2022. Assoc. Editor: Ning Zhang.

opening angle affect the turbine performance. Venters et al. [18] used a CFD-AD approach to find an optimized design for a DWT. They employed two objective functions for the optimization: one based on rotor power coefficient and the other on total power coefficient. That study was continued by Sadeghi et al. [19] using new optimization algorithms.

These computational studies gave a lot of helpful guidance on the design of DWTs. However, the aforementioned methods inevitably bear significant simplifications on the turbine geometries. Nowadays, it is viable to simulate fluid flows about real turbines using more advanced CFD techniques. Furthermore, the development of high-order methods made it possible to simulate a flow field at higher spatial accuracies than traditional finite volume methods. The most popular high-order methods include the discontinuous Galerkin method [20,21], the spectral element method [22,23], the spectral difference (SD) method [24–27], and the flux reconstruction (FR) method [28–30]. The SD and the FR methods are based on the differential-form governing equations and are two of the most efficient high-order methods. The FR method is a unified framework that can recover many existing high-order schemes (e.g., discontinuous Galerkin and SD schemes) and produce new schemes that were never reported before. To deal with rotating objects, Zhang and Liang [31,32] introduced the curved dynamic mortar concept and applied it to developing high-order sliding-mesh SD and FR methods. These methods were later extended to sliding-deforming meshes [33], 3D geometries [34], and general nonuniform sliding interfaces [35]. Zhang and Liang [36] further introduced the transfinite mortar concept that has no geometric error and makes a sliding-mesh method arbitrary high-order accurate in space and high-order in time. This method has been applied to simulate flows around rotating cylinders of different cross-sectional shapes [37], flapping wings for energy harvesting [38], and, more recently, the first high-order eddy-resolving simulation of flow over a marine propeller [39].

The authors of this work also applied the above techniques to a preliminary study of a DWT (designed at Clarkson University by Dr. Kenneth Visser) at its design condition [40]. In this work, we further study by comparing the DWT with the corresponding open-rotor wind turbine (OWT) at different working conditions. Given that DWTs can be installed in urban areas where the directions of winds may be affected by buildings, simulations for the DWT and OWT under yawed inflows are also performed.

The rest of this paper is organized as follows. Section 2 briefly introduces the numerical methods. Section 3 describes the simulation setup and the numerical validation. In Sec. 4, computations for turbines under axial flows are carried out, and results on the aerodynamic loads and flow fields are presented and analyzed. Section 5 reports simulation results for the yawed cases. Finally, Sec. 6 concludes this paper.

2 Numerical Methods

2.1 The Governing Equations. The three-dimensional unsteady Navier–Stokes equations in the following conservative form are numerically solved:

$$\frac{\partial \mathbf{Q}}{\partial t}+\frac{\partial \mathbf{F}}{\partial x}+\frac{\partial \mathbf{G}}{\partial y}+\frac{\partial \mathbf{H}}{\partial z}=\mathbf{0} \tag{1}$$

where $\mathbf{Q}$ is the vector of conservative variables, $\mathbf{F}$, $\mathbf{G}$, and $\mathbf{H}$ are the flux vectors in each coordinate direction. These terms have the following expressions:

$$\mathbf{Q}=[\rho\ \rho u\ \rho v\ \rho w\ E]^{\top} \tag{2}$$

$$\mathbf{F}=\mathbf{F}_{\text{inv}}(\mathbf{Q})+\mathbf{F}_{\text{vis}}(\mathbf{Q},\nabla\mathbf{Q}) \tag{3}$$

$$\mathbf{G}=\mathbf{G}_{\text{inv}}(\mathbf{Q})+\mathbf{G}_{\text{vis}}(\mathbf{Q},\nabla\mathbf{Q}) \tag{4}$$

$$\mathbf{H}=\mathbf{H}_{\text{inv}}(\mathbf{Q})+\mathbf{H}_{\text{vis}}(\mathbf{Q},\nabla\mathbf{Q}) \tag{5}$$

where ρ is fluid density, u, v, and w are the velocity components, E is the total energy per unit volume defined as $E=p/(\gamma-1)+1/2(\rho(u^2+v^2+w^2))$, p is pressure, and γ is the ratio of specific heats which is set to 1.4 in this work. The fluxes have been split into inviscid and viscous parts. The inviscid fluxes are only functions of the conservative variables and have the following expressions:

$$\mathbf{F}_{\text{inv}}=[\rho u\ \rho u^2+p\ \rho uv\ \rho uw\ u(E+p)]^{\top} \tag{6}$$

$$\mathbf{G}_{\text{inv}}=[\rho v\ \rho uv\ \rho v^2+p\ \rho vw\ v(E+p)]^{\top} \tag{7}$$

$$\mathbf{H}_{\text{inv}}=[\rho w\ \rho uw\ \rho vw\ \rho w^2+p\ w(E+p)]^{\top} \tag{8}$$

The viscous fluxes are functions of the conservative variables and the gradients. Their expressions are

$$\mathbf{F}_{\text{vis}}=-[0\ \tau_{xx}\ \tau_{yx}\ \tau_{zx}\ u\tau_{xx}+v\tau_{yx}+w\tau_{zx}+\kappa T_x]^{\top} \tag{9}$$

$$\mathbf{G}_{\text{vis}}=-[0\ \tau_{xy}\ \tau_{yy}\ \tau_{zy}\ u\tau_{xy}+v\tau_{yy}+w\tau_{zy}+\kappa T_y]^{\top} \tag{10}$$

$$\mathbf{H}_{\text{vis}}=-[0\ \tau_{xz}\ \tau_{yz}\ \tau_{zz}\ u\tau_{xz}+v\tau_{yz}+w\tau_{zz}+\kappa T_z]^{\top} \tag{11}$$

where τ_{ij} is the viscous stress tensor which is related to velocity gradients as $\tau_{ij}=\mu(u_{i,j}+u_{j,i})+\lambda\delta_{ij}u_{k,k}$, μ is the dynamic viscosity, $\lambda=-2/3(\mu)$ based on Stokes' hypothesis, δ_{ij} is the Kronecker delta, κ is the thermal conductivity, T is temperature which is related to density and pressure through the ideal gas law $p=\rho RT$, and R is the gas constant.

2.2 The Computational Equations. Each mesh element in the physical space is mapped to a standard element in a computational space. Assume the mapping is: $t=\tau$, $x=x(\tau,\xi,\eta,\zeta)$, $y=y(\tau,\xi,\eta,\zeta)$, and $z=z(\tau,\xi,\eta,\zeta)$, where (τ,ξ,η,ζ) are the computational time and coordinates. It can be shown that the governing equations will take the following conservative form in the computational space:

$$\frac{\partial \tilde{\mathbf{Q}}}{\partial t}+\frac{\partial \tilde{\mathbf{F}}}{\partial \xi}+\frac{\partial \tilde{\mathbf{G}}}{\partial \eta}+\frac{\partial \tilde{\mathbf{H}}}{\partial \zeta}=\mathbf{0} \tag{12}$$

The computational variables and fluxes are related to the physical ones as

$$\begin{bmatrix}\tilde{\mathbf{Q}}\\ \tilde{\mathbf{F}}\\ \tilde{\mathbf{G}}\\ \tilde{\mathbf{H}}\end{bmatrix}=|\mathcal{J}|\mathcal{J}^{-1}\begin{bmatrix}\mathbf{Q}\\ \mathbf{F}\\ \mathbf{G}\\ \mathbf{H}\end{bmatrix} \tag{13}$$

where $\mathcal{J}$ is the Jacobian matrix, $|\mathcal{J}|$ is the determinant, and $\mathcal{J}^{-1}$ is the inverse Jacobian matrix, of the mapping.

Besides the flow equations, the geometric conservation law [41] also needs to be numerically satisfied to ensure freestream preservation on moving grids. The detailed steps employed to solve the geometric conservation law equations in this work can be found in, e.g., Ref. [33].

2.3 The Flux Reconstruction Method. Only hexahedral elements are used in this work, and each element is mapped to a unit computational element $0\le\xi,\eta,\zeta\le 1$ via isoparametric mapping [42]. Solution points (SPs, denoted by X_s) are defined inside each computational element, and flux points (FPs, denoted by X_f) are then defined on the boundaries. The readers are referred to Fig. 2

in Ref. [36] or Fig. 1 in Ref. [39], for examples, of the SP and FP distributions. For an Nth-order FR scheme, there are N SPs and N FPs in each direction. The SPs and FPs are chosen as the Legendre points in this study.

At the SPs, the following Lagrange interpolation bases can be defined (where X_i is the coordinate of the ith SP)

$$h_i(X) = \prod_{s=1,s\neq i}^{N} \left(\frac{X - X_s}{X_i - X_s}\right), \quad i = 1, 2, \ldots, N \tag{14}$$

The above polynomials also form a basis for polynomials of degrees less than or equal to $N-1$, i.e., $\mathbf{P}_{N-1}$. The solution and fluxes within each element can be approximated via tensor products of the interpolation bases, e.g.,

$$\tilde{\mathbf{Q}}(\xi, \eta, \zeta) = \sum_{i=1}^{N}\sum_{j=1}^{N}\sum_{k=1}^{N} \tilde{\mathbf{Q}}_{ijk} h_i(\xi) h_j(\eta) h_k(\zeta) \tag{15}$$

$$\tilde{\mathbf{F}}(\xi, \eta, \zeta) = \sum_{i=1}^{N}\sum_{j=1}^{N}\sum_{k=1}^{N} \tilde{\mathbf{F}}_{ijk} h_i(\xi) h_j(\eta) h_k(\zeta) \tag{16}$$

where the subscript ijk denotes the discrete value at the (i, j, and k)th SP. Obviously, the solution and flux polynomials are in $\mathbf{P}_{N-1,N-1,N-1}$ and are continuous within each element but discontinuous across cell boundaries. Therefore, common values need to be defined at cell boundaries. In this work, the common solution is calculated as the average of the discontinuous values from the two sides of a boundary; the common inviscid fluxes are computed using the Rusanov solver [43]; the common viscous fluxes are computed from the common solutions and common gradients.

After taking the spatial derivatives in Eq. (12), the three flux terms are reduced to elements of $\mathbf{P}_{N-2,N-1,N-1}$, $\mathbf{P}_{N-1,N-2,N-1}$, and $\mathbf{P}_{N-1,N-1,N-2}$, respectively, which are inconsistent with the solution term. To fix this issue, the degrees of the original flux polynomials need to be raised, which can be achieved using higher-degree correction functions [28]. For example, the corrected/reconstructed flux in the ξ direction is

$$\begin{aligned}\hat{\mathbf{F}} = \tilde{\mathbf{F}}(\xi, \eta, \zeta) &+ [\tilde{\mathbf{F}}^{\text{com}}(0, \eta, \zeta) - \tilde{\mathbf{F}}(0, \eta, \zeta)] \cdot g_L(\xi) \\ &+ [\tilde{\mathbf{F}}^{\text{com}}(1, \eta, \zeta) - \tilde{\mathbf{F}}(1, \eta, \zeta)] \cdot g_R(\xi)\end{aligned} \tag{17}$$

where $\tilde{\mathbf{F}}$ is from Eq. (16), $\tilde{\mathbf{F}}^{\text{com}}$ is the common flux on a cell boundary, and g_L and g_R are the left and the right correction functions that are required to satisfy

$$g_L(0) = 1, \quad g_L(1) = 0, \quad g_R(0) = 0, \quad g_R(1) = 1 \tag{18}$$

These conditions ensure that the reconstructed flux still takes the common values on cell boundaries. In this work, the g_{DG} function [28] is chosen as the correction function. The other two fluxes are reconstructed in the same way. Finally, the reconstructed fluxes are used to compute the residuals and then to update the solutions. For temporal discretization, a four-stage third-order explicit Runge–Kutta method [44,45] is employed.

2.4 The Sliding-Mesh SD/FR Method. There are two fundamental types of sliding interfaces in 3D (the readers are referred to Fig. 2 in Ref. [39] for illustrations). For simplicity, we assume that the mesh points do not match in the azimuthal direction but match in the other direction. We further assume that the azimuthal direction is uniformly meshed. The second type is taken to briefly explain how the method works. More detailed explanation can be found in previous papers, e.g., Refs. [34,36], and [39].

Curved dynamic mortar elements [32] are employed to communicate between the two sides of a sliding interface. Base on the above assumptions, at each time instant, a cell face Ω is connected to two mortar elements Ξ_1 and Ξ_2 (see Fig. 3 in Ref. [39]). These curved geometries are mapped to straight ones first. For Ω, assume that the azimuthal direction is mapped to ξ and the other direction is mapped to η in the computational space. Similarly, for each mortar, assume these two directions are mapped to ξ' and η', respectively, in the mortar space. Then these two spaces are related as: $\xi = o + s \cdot \xi'$, $\eta = \eta'$, where $0 \le \xi, \eta, \xi', \eta' \le 1$, and o and s are the offset and scaling of a mortar with respect to a cell face.

Any variables ϕ^{Ω} (on a cell face Ω) and $\phi^{\Xi,L}$ (on the left side of a mortar Ξ) can be represented by polynomials similar to those in Eqs. (15) and (16), but in two-dimensional. To get $\phi^{\Xi,L}$, we require (see Fig. 4(a) in Ref. [39])

$$\begin{aligned}&\int_0^1\int_0^1 (\phi^{\Xi,L}(\xi', \eta') - \phi^{\Omega}(\xi, \eta)) h_\alpha(\xi') h_\beta(\eta') \mathrm{d}\xi' \mathrm{d}\eta' = 0, \\ &\forall \alpha, \beta = 1, 2, \ldots, N\end{aligned} \tag{19}$$

The same process is repeated on the right side of the mortar. After that, a common value, denoted as Φ, are computed on mortars and then projected back to cell faces (see Fig. 4(b) in Ref. [39]) according to

$$\begin{aligned}&\sum_{k=1}^{2} \int_{\xi=o_k}^{\xi=o_k+s_k} \int_{\eta=0}^{\eta=1} (\Phi^{\Omega}(\xi, \eta) - \Phi^{\Xi_k}(\xi', \eta')) h_\alpha(\xi) h_\beta(\eta) \mathrm{d}\xi \mathrm{d}\eta = 0, \\ &\forall\, \alpha, \beta = 1, \ldots, N\end{aligned} \tag{20}$$

It can be shown that the two projections, Eqs. (19) and (20), are equivalent to a series of one-dimensional projections [46], which make the process very efficient.

3 Simulation Setup

3.1 Geometry. The DWT considered here was designed at Clarkson University by Dr. Kenneth Visser [47]. Figure 1 shows two views of the geometry and a photo of the real product. The diffuser duct has a profile of the E423 high lift airfoil, with an inlet radius of $R_i = 1.546$ m, an exit radius of $R_o = 1.832$ m, a width of $W = 0.612$ m, and an angle of attack of $\alpha = 25$ deg. The rotor has three 1.5 m-long blades (i.e., $R_b = 1.5$ m) that are 0.388 m downstream from the inlet. More information about the blade shape can be found in Ref. [47]. The cylindrical hub has a diameter of $D_h = 0.456$ m and is closed by two hemispherical ends of the same diameter. This configuration results in a small gap of approximately 0.113 m between the blade tips and the duct's inner surface.

3.2 Meshes and Boundary Conditions. Figure 2(a) shows the surface meshes of the DWT's wall boundaries. Along these boundaries, the first layer of volume mesh has a height of approximately $3 \times 10^{-3} D_o$, and the first layer of solution points is about $1.4 \times 10^{-4} D_o$ off the walls (for a fifth-order scheme), where $D_o = 2R_o$ is the diameter of the duct's exit. Figure 2(b) shows the meshes on the upstream sliding interface and the duct's inner surface. In fact, there are two sliding interfaces, and the other one is downstream at the duct's exit. Because the gap between the blade tips and the duct's inner surface is too small to allow a third sliding interface there, the duct's inner surface is set to rotate with the two sliding interfaces. The speed on this inner surface is then overwritten to zero. The surface mesh of the OWT's rotor is identical to that of the DWT. The OWT allows three sliding interfaces that form a disk region, as shown in Fig. 2(c). This region has a thickness of W (please refer to Fig. 1(b) for the value) and diameter of $1.5D_o$. For both turbines, the hubs and their ends rotate at the same angular speed as the blades.

The overall computational domain for the DWT has a cylindrical shape, as shown in Fig. 3(a). The length and diameter of the

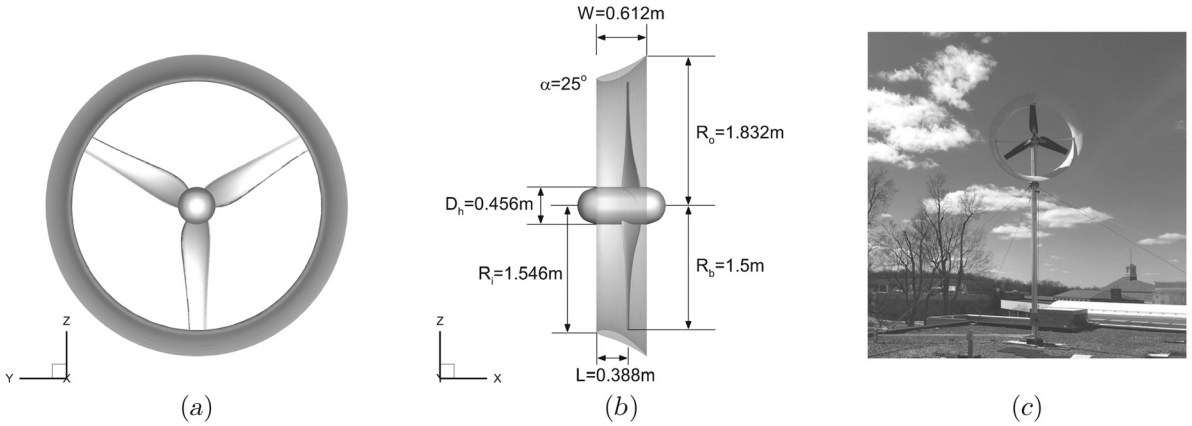

Fig. 1 The DWT geometry: (*a*) upstream view, (*b*) lateral view, and (*c*) photo of a real product

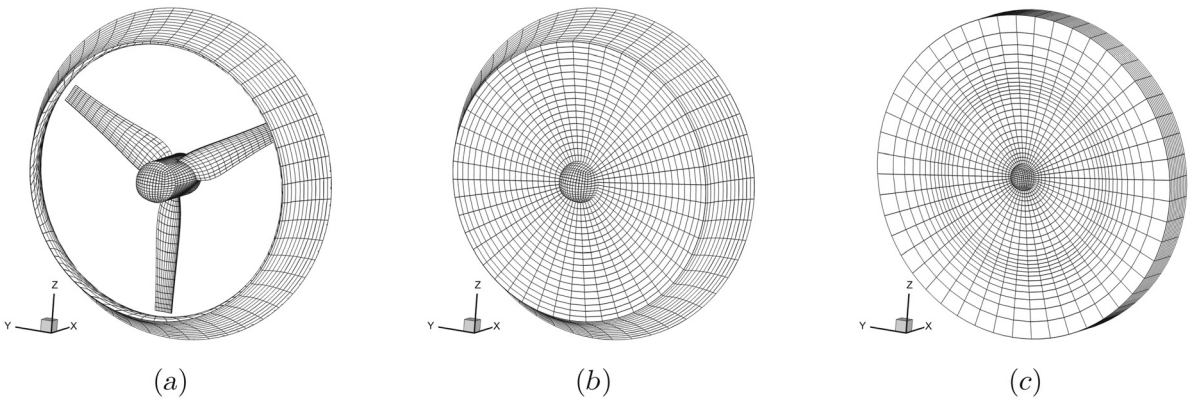

Fig. 2 (*a*) The DWT surface mesh, (*b*) the DWT sliding interface mesh, and (*c*) the OWT sliding interface mesh

domain are both $12D_o$. The domain for the OWT has the same shape and size. The resulting blockage ratio is 0.69% for the DWT and 0.47% for the OWT. The overall mesh with a 1/4 cutout is shown in Fig. 3(*b*), where the red area (color online) represents a sliding subdomain. For the DWT, the sliding subdomain has 29,469 elements, and the outer subdomain has 266,969 elements, resulting in 296,438 total elements (or 37.1×10^6 degrees-of-freedom (DOFs) for a fifth-order scheme). For the OWT, the sliding region has 54,432 elements, and the outer subdomain has 240,905 elements, adding up to 295,337 elements in total (or 37.0×10^6 DOFs for a fifth-order scheme). The domain inlet is treated as a Dirichlet boundary. The outlet and outer cylindrical surface are treated as characteristic farfields. All solid walls are treated as no-slip adiabatic walls. The Mach number of the incoming freestream flow is set to $\mathrm{Ma}_\infty = 0.08$ to ensure negligible compressibility effect.

3.3 Physical and Nondimensional Parameters. The most common physical operating conditions for the present DWT are listed in Table 1. Once the geometry of the turbine is given, there are two nondimensional parameters that govern the flow. One is the Reynolds number Re, and the other is the tip speed ratio λ. In this study, we adopt the following definitions:

$$\mathrm{Re} = \frac{U_\infty D_o}{\nu} \quad \text{and} \quad \lambda = \frac{\omega R_b}{U_\infty} \tag{21}$$

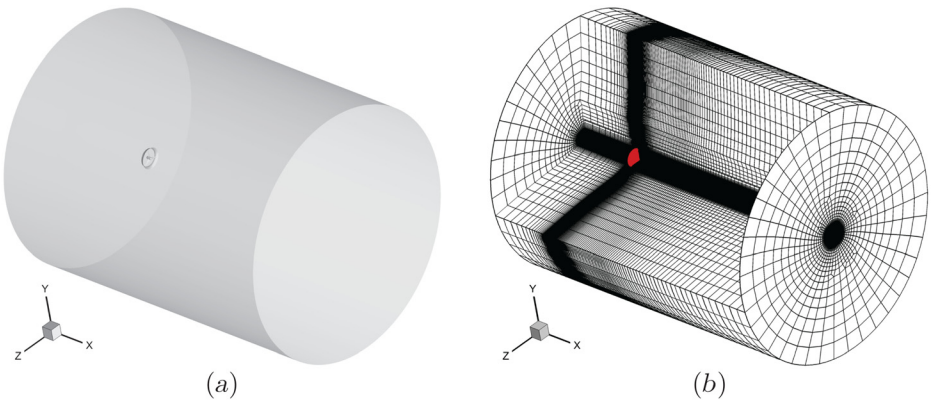

Fig. 3 Overall computational domain and mesh: (*a*) domain and (*b*) mesh

Table 1 Physical operating conditions

Parameter	Value
Freestream velocity (U_∞)	10 m/s
Kinematic viscosity (ν)	1.4616×10^{-5} m^2/s
Rotation axis	x-direction
Rotation speed (ω)	–26.18 rad/s

Table 2 Results from different scheme orders

	$N=4$	$N=5$	$N=6$
$\bar{C}_T$	5.31×10^{-1}	6.02×10^{-1}	6.34×10^{-1}
$\bar{C}_P$	2.74×10^{-1}	3.74×10^{-1}	4.02×10^{-1}

The values in Table 1 give Re $= 2.5 \times 10^6$ and $\lambda = 3.93$. Hereinafter, the Reynolds number is kept constant for all the cases. Two more values, $\lambda = 3.11$ and $\lambda = 4.75$, are studied for some cases to examine the effects of the tip speed ratio.

In what follows, all the simulations use a small nondimensional time-step size of $\Delta t^* = \Delta t U_\infty / D_o = 1.25 \times 10^{-5}$ for stability consideration. This time-step size corresponds to a blade rotation between 0.0054 deg (for $\lambda = 3.11$) and 0.0083 deg (for $\lambda = 4.75$), which is small enough to provide sufficient sampling resolution. Each simulation was run for 25 nondimensional time units, and data sets from the last 12.5 time units were used to calculate the statistics.

3.4 Verification and Validation. For the method used, the total number of DOFs is $N_{\text{DOF}} = N_{\text{elem}} \cdot N^3$, where N_{elem} is the total number of mesh elements, and N is the scheme order. Once a mesh is generated, we can vary the scheme order N to identify the resolution requirement for a simulation. The Reynolds number in this study is extremely high, which makes it prohibitively expensive to get fully resolved solutions (i.e., to resolve turbulent eddies of all sizes). Thus, we need to identify a proper scheme order that gives a good balance between computational cost and solution qualities.

To do this, we employ the thrust coefficient C_T and power coefficient C_P as two measurement criteria. These two terms are defined as below

$$C_T = \frac{T}{\frac{1}{2}\rho U_\infty^2 A_{\text{rot}}}, \quad C_P = \frac{Q\omega}{\frac{1}{2}\rho U_\infty^3 A_{\text{rot}}} \tag{22}$$

where T and Q, respectively, are the thrust (in fact drag for a turbine) and the torque (only the x-component) acted on turbine blades, and $A_{\text{rot}} = \pi R_b^2$ is the swept area of rotor blades.

Three scheme orders, $N=4$, 5, and 6, are applied to the OWT at the operating conditions listed in Table 1. The time-averaged results are summarized in Table 2. It is observed that the $\bar{C}_T$'s from $N=4$ and 5 are 16% and 5%, respectively, smaller than that from $N=6$. Meanwhile, the $\bar{C}_P$'s from $N=4$ and 5 are 32% and 7%, respectively, smaller than that from $N=6$. The data obviously shows a converging trend as N increases. Going from $N=5$ to $N=6$ increases the computational cost by 73%, but the changes in the coefficients are relatively small. Thus $N=5$ is chosen as the scheme order to perform the simulations.

While, there is no direct experimental data available on the present turbines for validation purpose, the present numerical methods and flow solver have been validated on several flows in our previous works. For example, they have been validated on the DTMB 4119 propeller, where excellent agreement between experiment and simulation was obtained. Interested readers are referred to Ref. [39] for the validation results.

4 Simulation of Turbines in Axial Flows

In this section, the results and analysis for the axial flow cases are presented, in which the freestream moves along the turbines' axial direction. Besides the designed tip speed ratio $\lambda = 3.93$ (i.e., $\omega^* = \omega D_o / U_\infty = -9.60$), two other tip speed ratios: $\lambda = 3.11$ (i.e., $\omega^* = -7.60$) and $\lambda = 4.75$ (i.e., $\omega^* = -11.60$) are considered, and the loads, vortex fields and velocity fields are analyzed.

4.1 Load Analysis. Figure 4 shows the time histories of C_T and C_P for the two configurations at the designed tip speed ratio. It is seen that the thrust and power outputs for both configurations are well converged, and the DWT's loads have larger fluctuations than those of the OWT, which indicates that the flow over the DWT is more turbulent.

The mean (time-averaged) values, r.m.s (root-mean-square) deviations, and the corresponding contributions from pressure (with subscript p) and viscosity (with subscript v) of the loads are listed in Table 3. Overall, the r.m.s values are about two orders of magnitude smaller than the mean values, suggesting that the loads are relatively steady. Meanwhile, viscosity contributions are over

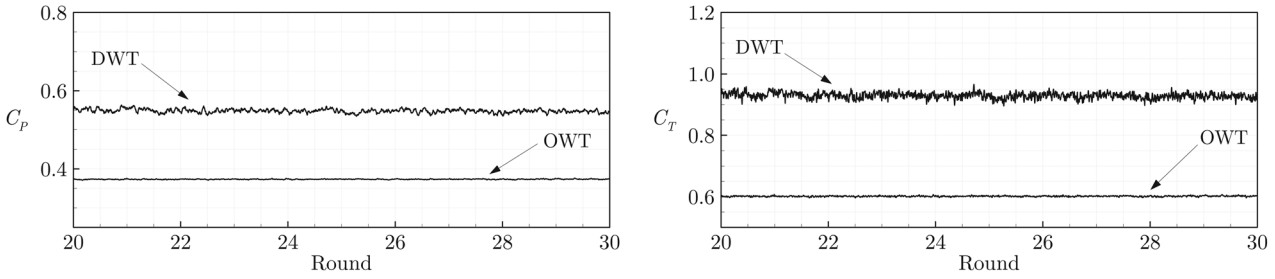

Fig. 4 Time histories of the loads for the two configurations at $\lambda = 3.93$

Table 3 Loads and their components of the two turbines at λ=3.93

		C_T	$C_{T,p}$	$C_{T,v}$	C_P	$C_{P,p}$	$C_{P,v}$
DWT	Mean	9.28×10^{-1}	9.28×10^{-1}	1.97×10^{-4}	5.47×10^{-1}	5.49×10^{-1}	-1.20×10^{-3}
	r.m.s	9.79×10^{-3}	9.79×10^{-3}	5.79×10^{-7}	4.87×10^{-3}	4.87×10^{-3}	8.27×10^{-6}
OWT	Mean	6.02×10^{-1}	6.01×10^{-1}	1.91×10^{-4}	3.74×10^{-1}	3.75×10^{-1}	-1.44×10^{-3}
	r.m.s	1.55×10^{-3}	1.55×10^{-3}	5.41×10^{-7}	7.38×10^{-4}	7.39×10^{-4}	1.45×10^{-6}

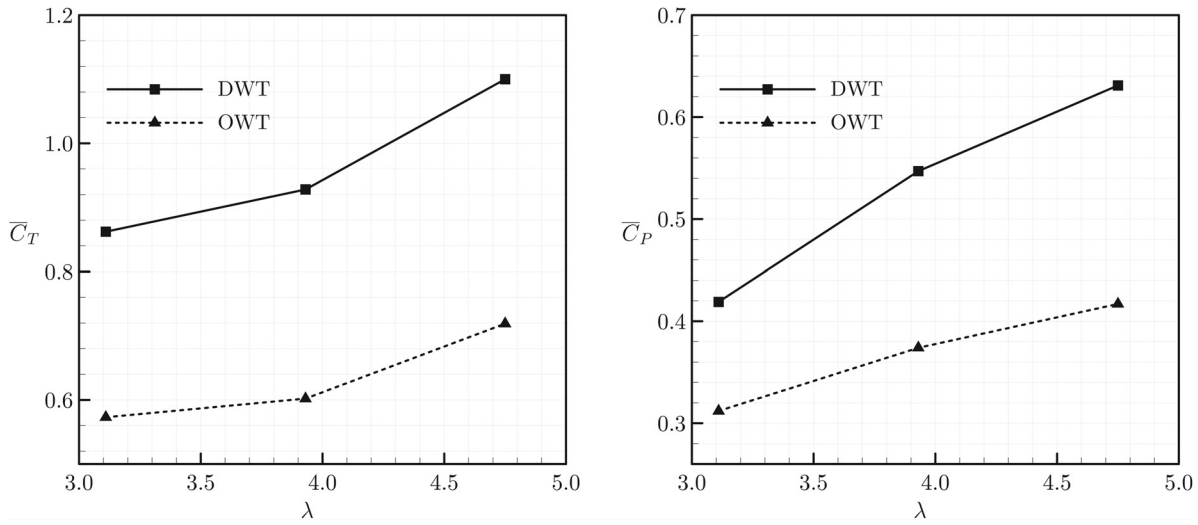

Fig. 5 Mean loads at different tip-speed ratios

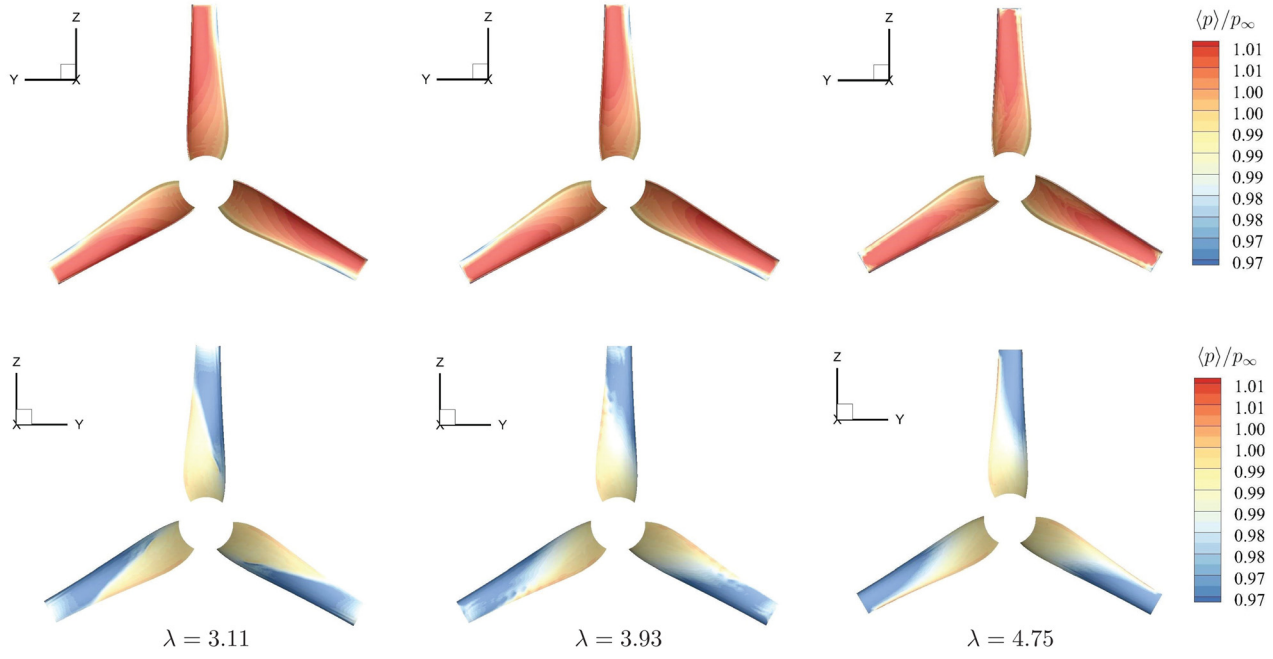

Fig. 6 The DWT's phase-averaged surface pressure: top, upstream; bottom, downstream

three orders of magnitude smaller than pressure contributions for C_T, and about two orders of magnitude smaller for C_P, revealing that pressure plays a much dominant role on the loads. Moreover, viscosity has positive contributions to the mean thrust but negative contributions to the power output. Most interestingly, the DWT's mean thrust coefficient is about 54% higher, and the mean power coefficient is about 46% higher than the OWT's.

The time-averaged load coefficients (denoted by $\bar{C}_T$ and $\bar{C}_P$) at the three tip speed ratios are shown in Fig. 5. For both turbines, $\bar{C}_T$ and $\bar{C}_P$ increase with λ in this range. The $\bar{C}_T$'s for both turbines grow at almost the same pace (with a difference of approximately 0.3 between the two curves), while the $\bar{C}_P$ of the DWT grows faster than that of the OWT.

The phase-averaged pressure on the blade surfaces is plotted to show more details of the load distributions on the blades. As shown in Fig. 6, for the DWT, the upstream surface experiences a higher pressure than the downstream surface. Thus, the rotor experiences a drag force pointed toward the x-direction. The outboard part of the blades, especially the area around the leading edge, has a higher pressure difference, which means the load strength is higher in this region. The OWT's phase-averaged pressure contours are given in Fig. 7. A similar pressure distribution as that of the DWT is observed. One major difference is that the downstream surface has a smaller area of low pressure than that of the DWT, which is responsible for the smaller loads than the DWT's.

The phase-averaged pressure at $x/D = 0.02$ for both turbines is shown in Fig. 8. Due to the pressure difference between the two sides of each blade, each blade experiences a torque pointed toward the negative x-axis. This torque direction is the same as the rotation direction, which means positive work is done to the rotor, and the wind energy is transferred to the rotor's mechanical energy. The major difference between the two turbines is still that the DWT has larger low-pressure regions.

4.2 Vortex Fields. Isosurfaces of instantaneous Q-criterion, colored by the streamwise velocity, are plotted in Fig. 9 for both

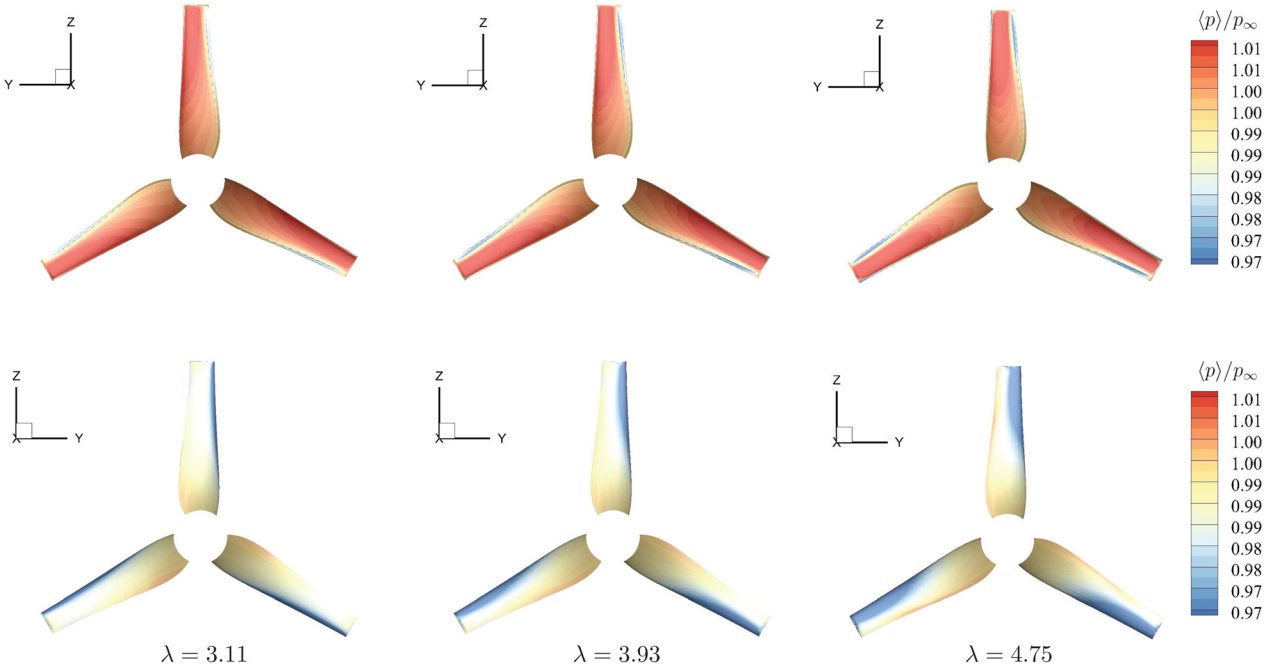

Fig. 7 The OWT's phase-averaged surface pressure: top, upstream; bottom, downstream

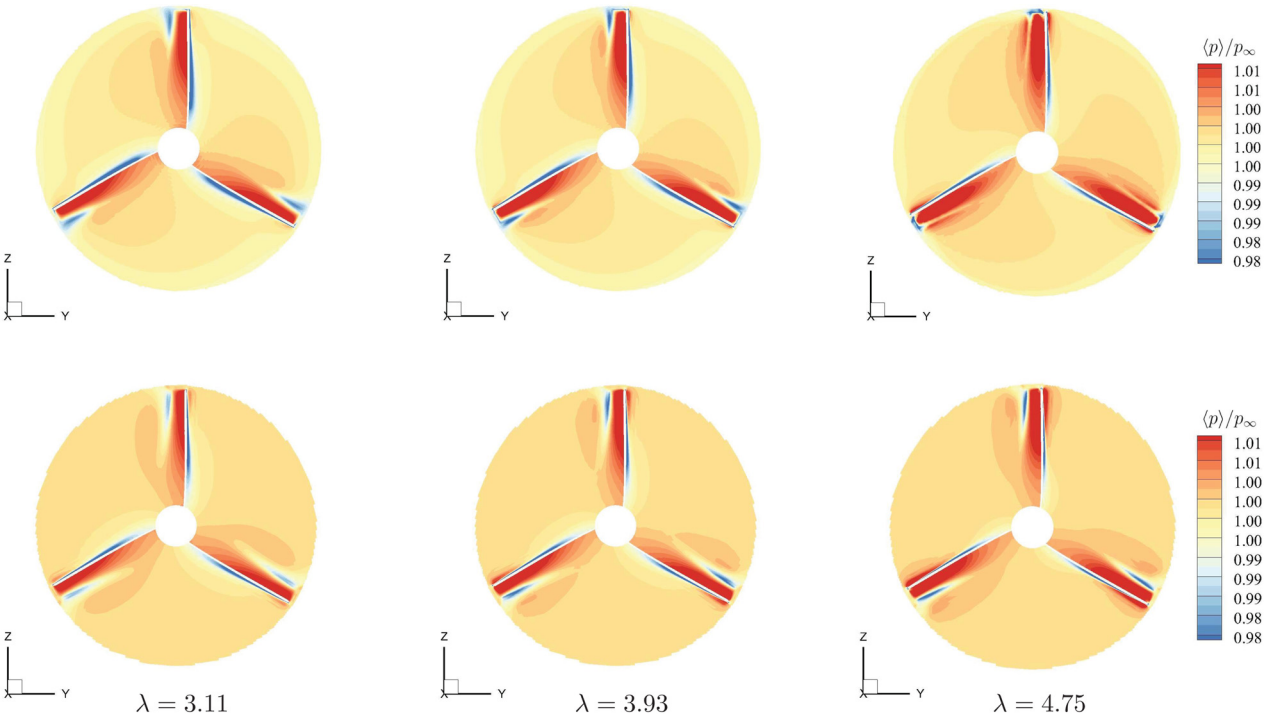

Fig. 8 Phase-averaged pressure at $x/D = 0.02$: top, DWT; bottom, OWT

turbines. A view through the central plane of the DWT at $\lambda = 3.93$ is shown in Fig. 10. Compared with the OWT's flow fields, there are dramatic changes in the DWT's due to the addition of the duct. Several important observations can be made. For example, (1) the DWT's flow fields are much wider in the radial direction; (2) the flow fields are more turbulent with a much broader range of flow structures; (3) tip vortices have been dramatically weakened and can hardly be observed; (4) hub vortices have almost been entirely suppressed; and (5) the blades' trailing-edge vortices have been enhanced (see Fig. 10).

4.3 Velocity Fields. Contours of the mean streamwise velocity, $\bar{u}$, in the central x–y plane are shown in Fig. 11 for the three tip speed ratios. It is seen that the flows downstream of both turbines are at reduced speeds compared with the freestream flow, which represents a fluid kinetic energy loss. The DWT's wakes have much larger low-speed regions than those of the OWT, indicating more fluid kinetic energy loss, which is consistent with the higher power coefficients of the DWT.

At $\lambda = 3.11$ and 3.93, the DWT's low-speed regions have similar diverging–converging shapes. However, at $\lambda = 4.75$, the

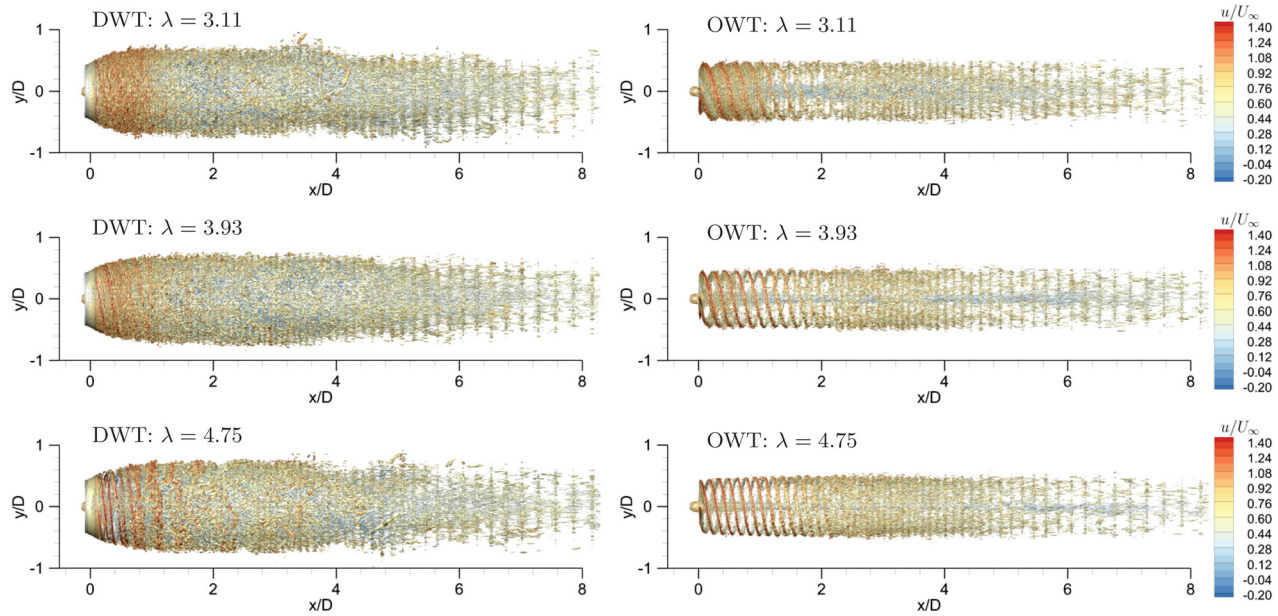

Fig. 9 Isosurface of instantaneous Q-criterion $Q_{cr}D^2/U_\infty^2 = 60$

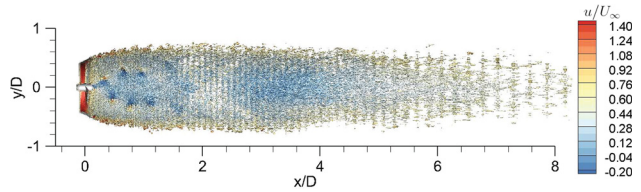

Fig. 10 Flow structures in the central *x–y* plane of the DWT at $\lambda = 3.93$

DWT's wake becomes bifurcated. It is conjectured that the bifurcation is caused by the blockage effects of the blades and the duct. From Fig. 1, it is observed that each blade is almost perpendicular to the incoming flow around the tip but more skewed (in other words, more aligned with the flow) toward the root. When a blade rotates faster (i.e., as λ increases), the tip blockage effect increases more substantially, which, when combined with the presence of the duct, dramatically reduces the flow speed downstream of the duct. It is worth mentioning that the gap between the tips and the duct's inner surface is too small (about $0.03D$) to allow much fluid to go through. Meanwhile, the enhanced blockage effect forces

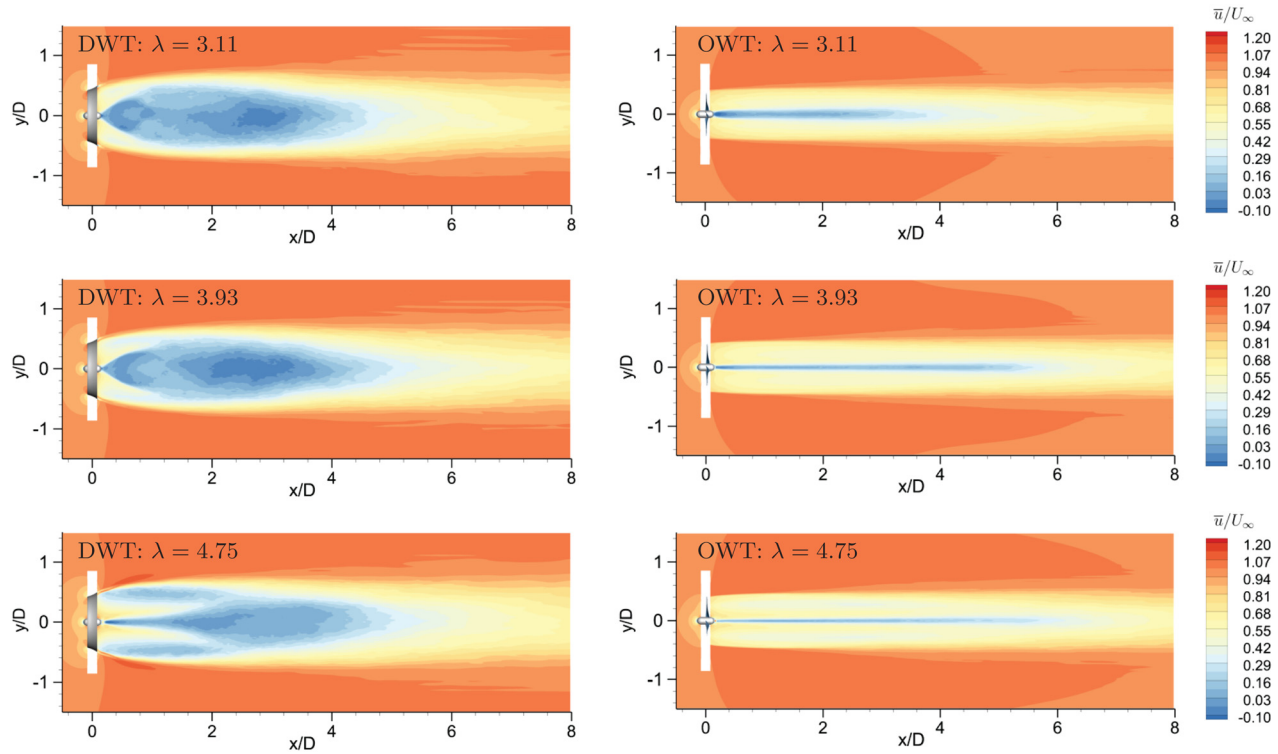

Fig. 11 Contours of mean streamwise velocity $\bar{u}$ in the central *x–y* plane

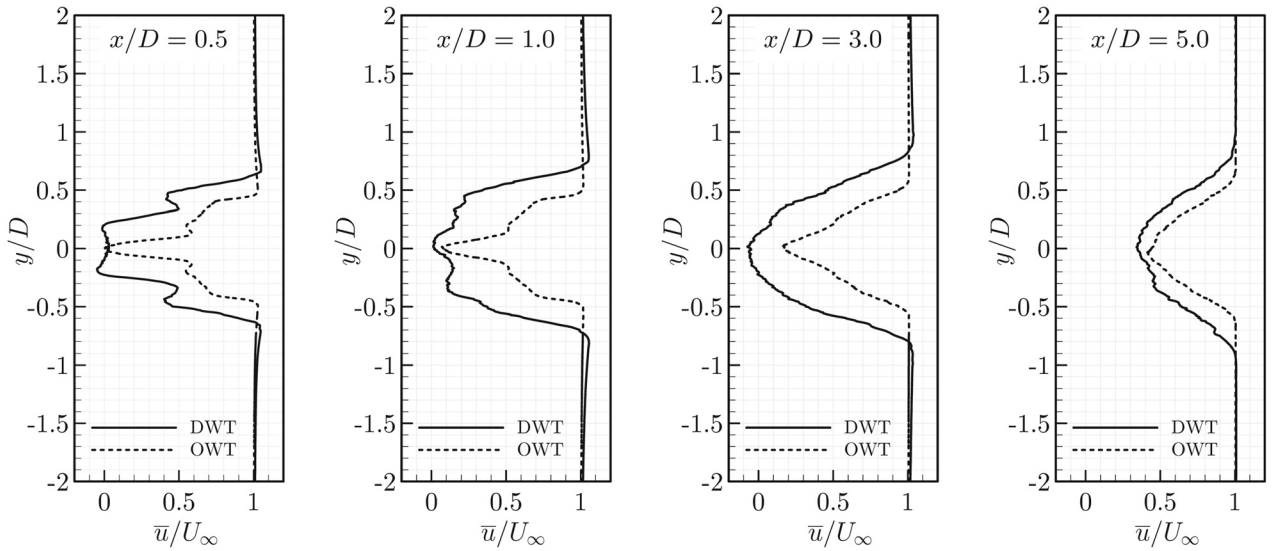

Fig. 12 Profiles of mean streamwise velocity for $\lambda = 3.11$ at different streamwise locations in the central *x–y* plane

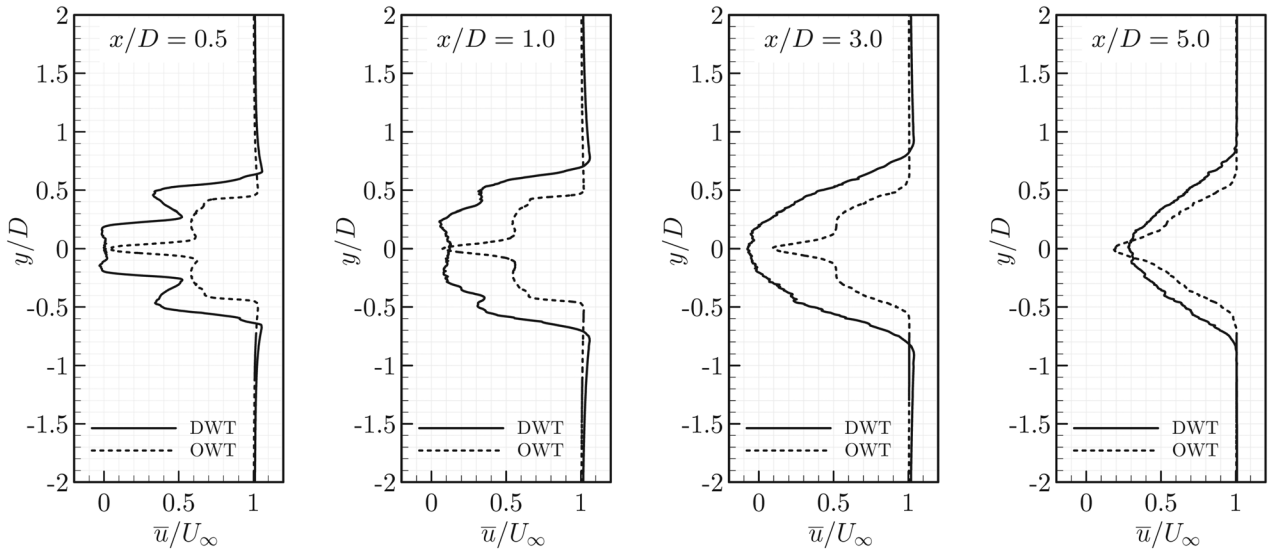

Fig. 13 Profiles of mean streamwise velocity for $\lambda = 3.93$ at different streamwise locations in the central *x–y* plane

more fluid to go through the root region of the blades, resulting in larger root flow speeds at $\lambda = 4.75$ than at $\lambda = 3.11$ and 3.93. The combination of the flows in these two regions (i.e., tips and roots) results in a bifurcation in the wake. The tip blockage effects actually also exist in the OWT's flow fields. As can be seen from the second column of Fig. 11, the flow speeds downstream of the OWT's tips also decrease as λ increases.

To quantitatively see how the wakes develop, we plot the mean streamwise velocity profiles in Figs. 12–14. Overall, the wakes show a consistent recovery trend as the flows travel downstream. At almost every location and for every λ, the DWT's wake has lower speeds than the OWT's. The notable exceptions are at $x/D = 5$ and for the $\lambda = 3.93$ and 4.75 cases, where the OWT's wakes have lower speeds around $y/D = 0$ because of the presence of strong hub vortices.

The effects of the blades and the duct on the wakes are most evident on the profiles at $x/D = 0.5$. Since the mean flow is symmetric about $y/D = 0$, we thus only focus on the $y/D > 0$ part to examine the effects. For the DWT, there is always a local minimum of $\bar{u}$ around $y/D = 0.5$, which is caused by the blockage effect of the duct. The value of this local minimum decreases as λ increases (the values are approximately 0.41, 0.32, and 0.19 for $\lambda = 3.11$, 3.93, and 4.75, respectively), suggesting an increasing blockage effect. Right below this minima is a local speed maximum. As λ increases, the maximum's location moves downward (toward the root), and its value increases. More specifically, their locations are $y/D = 0.33$, 0.28, and 0.14, and the corresponding values are 0.50, 0.52, and 0.66, respectively, for $\lambda = 3.11$, 3.93, and 4.75. These speed distributions agree with our conjecture that increasing the rotational speed will cause stronger tip and duct blockage effects and enhanced root flows, which are responsible for the wake bifurcation.

5 Simulation of Turbines in Yawed Flows

This section focuses on several yawed flows at $\lambda = 3.93$. To facilitate the discussion, besides the original physical coordinate system, we introduce a flow coordinate system x'–y' as shown in Fig. 15, where x' is along the freestream flow direction, and y' is perpendicular to the freestream flow direction. The yaw angle γ is defined as the angle between the flow direction and the axial direction of the turbine, i.e., the angle between x' and x. Four yaw

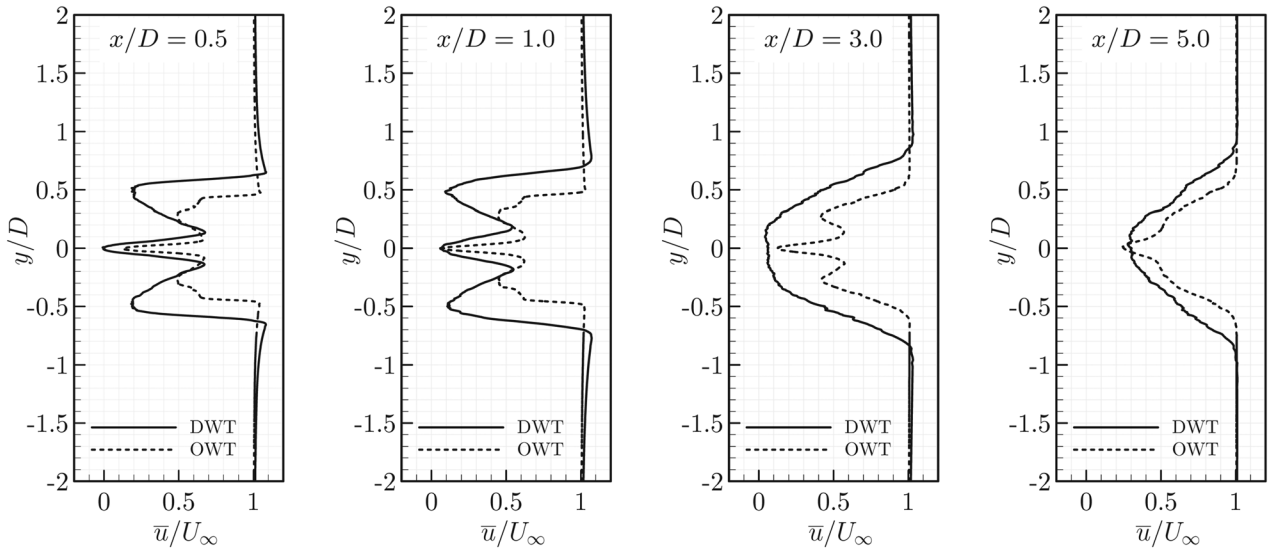

Fig. 14 Profiles of mean streamwise velocity for $\lambda = 4.75$ at different streamwise locations in the central *x–y* plane

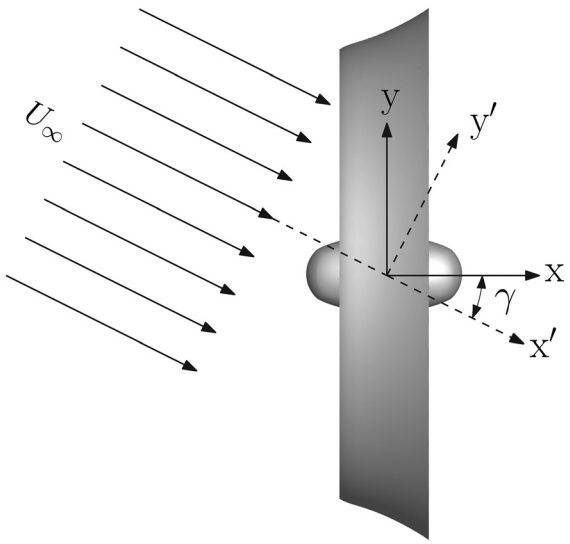

Fig. 15 Definitions of coordinates and yaw angle

angles: $\gamma = 0$ deg, 10 deg, 20 deg, and 30 deg are considered for both the DWT and the OWT. It is worth noting that because of axial symmetry, we do not consider the sign of the yaw angle here.

5.1 Load Analysis. The turbines' mean thrust and power coefficients at the four yaw angles are plotted in Fig. 16. It is seen that the DWT experiences more drag and extracts more energy than the OWT at all yaw angles. The DWT's performance is found to be insensitive to small yaw angles (e.g., for $\gamma < 10$ deg). Other than that, the two coefficients of both turbines decrease as the yaw angle increases, which is a direct result of the flowrate decrease across the turbines' swept areas.

To see the relative performance change at different yaw angles, we normalize both coefficients with their values at $\gamma = 0$ deg. The normalized coefficients are plotted in Fig. 17. Except for small yaw angles for the DWT, the yaw angle is found to have more substantial effects on the power coefficients than on the thrust coefficients. For example, from $\gamma = 0$ deg to $\gamma = 20$ deg, the OWT sees a 6% relative drop in the thrust coefficient but a 12% relative drop in the power coefficient. From $\gamma = 0$ deg to $\gamma = 30$ deg, the OWT experiences a 13% and 26% relative drop on the $\bar{C}_T$ and

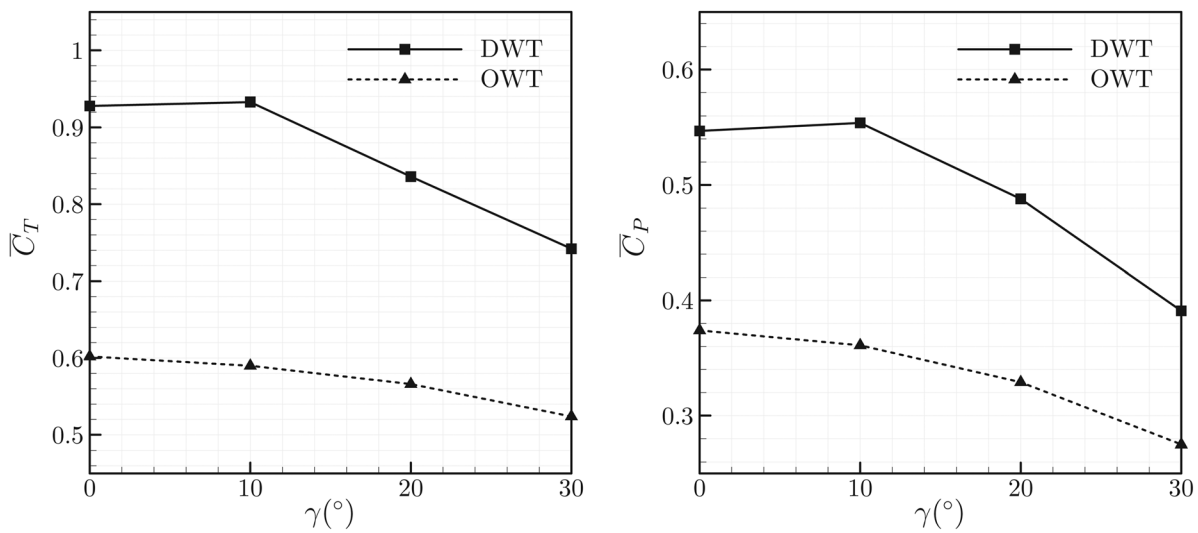

Fig. 16 Mean thrust and power coefficients for yawed flows at $\lambda = 3.93$

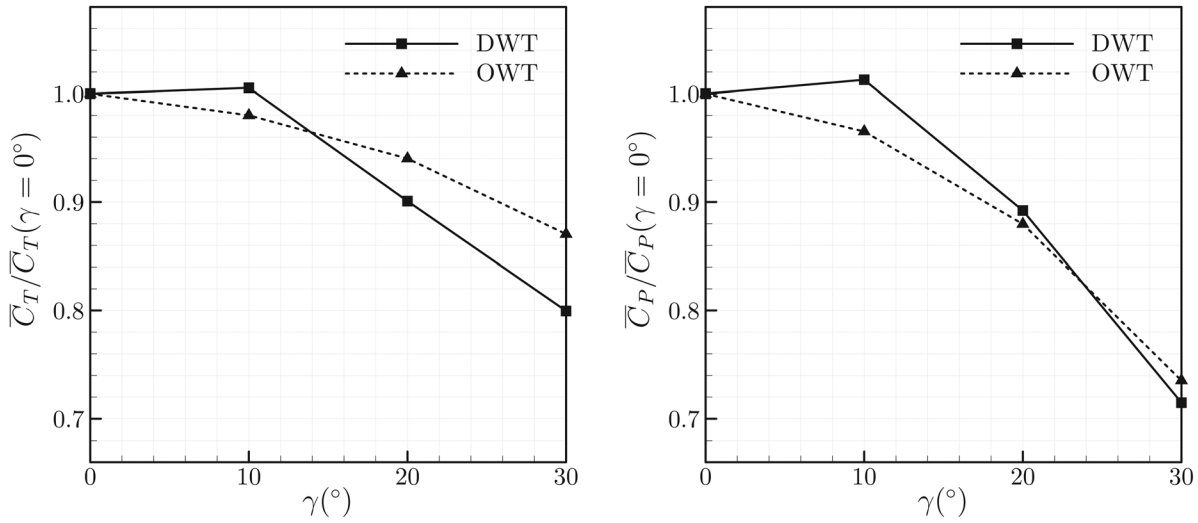

Fig. 17 Normalized mean thrust and power coefficients for yawed flows at $\lambda = 3.93$

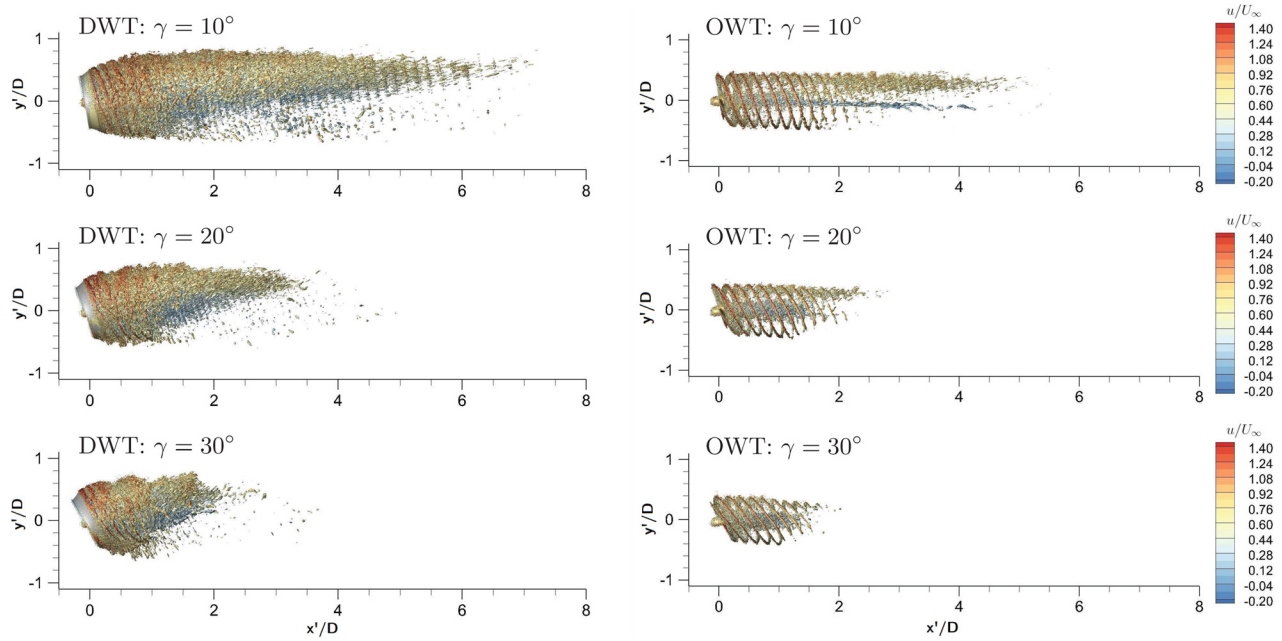

Fig. 18 Isosurfaces of the instantaneous Q-criterion $Q_{cr}D^2/U_\infty^2 = 60$ for yawed flows

$\bar{C}_P$, respectively, while the DWT sees a 20% and 29% relative drop in the two coefficients.

5.2 Vortex Fields. Isosurfaces of the instantaneous Q-criterion for the turbines are shown in Fig. 18. For simplicity and fair comparison, the plots are presented in the flow coordinates (i.e., the x'–y' coordinates). Obviously, nonzero yaw angles have made the wakes asymmetric about the flow direction. These asymmetries can be qualitatively explained as follows. In the extreme situation of infinitely large blade rotation speed, the flows are completely blocked in the turbines' cross section, and the turbines behave like two disks. At a finite rotational speed, the turbines still roughly behave like disks with some cross-sectional flow rates. The upper (leading) edges of the "disks" cause much larger flow separations than the lower (trailing) edges, resulting in the present asymmetric shapes of the wakes. Furthermore, as the yaw angle increases, the relative angle of attack of the "disks" decreases, resulting in weaker wake vortices. Of course, the blades' rotation motions add more complexities to the flow fields. For example, for the OWT, the spiral tip vortices are still present even for large yaw angles, but the hub vortices gradually disappear as the yaw angle increases.

5.3 Velocity Fields. Contours of the mean streamwise flow velocity in the central x'–y' plane at different yaw angles are plotted in Fig. 19. It is seen that the wakes are still at lower speeds compared with the freestream. However, the sizes of the low-speed regions decrease as the yaw angle increases, which agrees with the decreasing energy extraction performances revealed in Fig. 16. Although the results are presented in the flow coordinate, deflections of the wakes are still observed. Overall, the OWT shows more considerable wake deflections than the DWT. For the DWT, as the yaw angle increases, the angle of attack of the duct's upper portion increases, which has led to larger flow separations and larger blockage effects around the duct's upper trailing edge. Strong interactions are seen between the duct's upper wake and the DWT's main wake. For the duct's lower portion, the situation

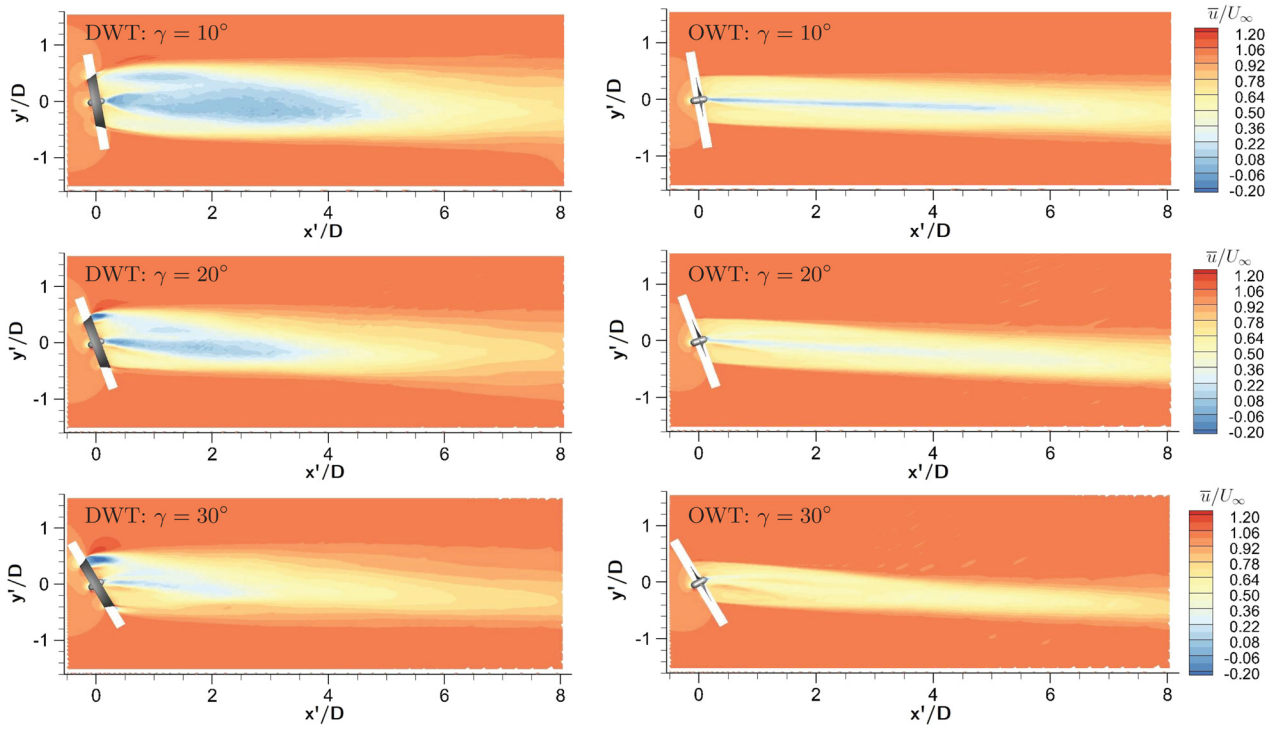

Fig. 19 Mean streamwise velocity contours at $\lambda = 3.93$ in the central x'–y' plane

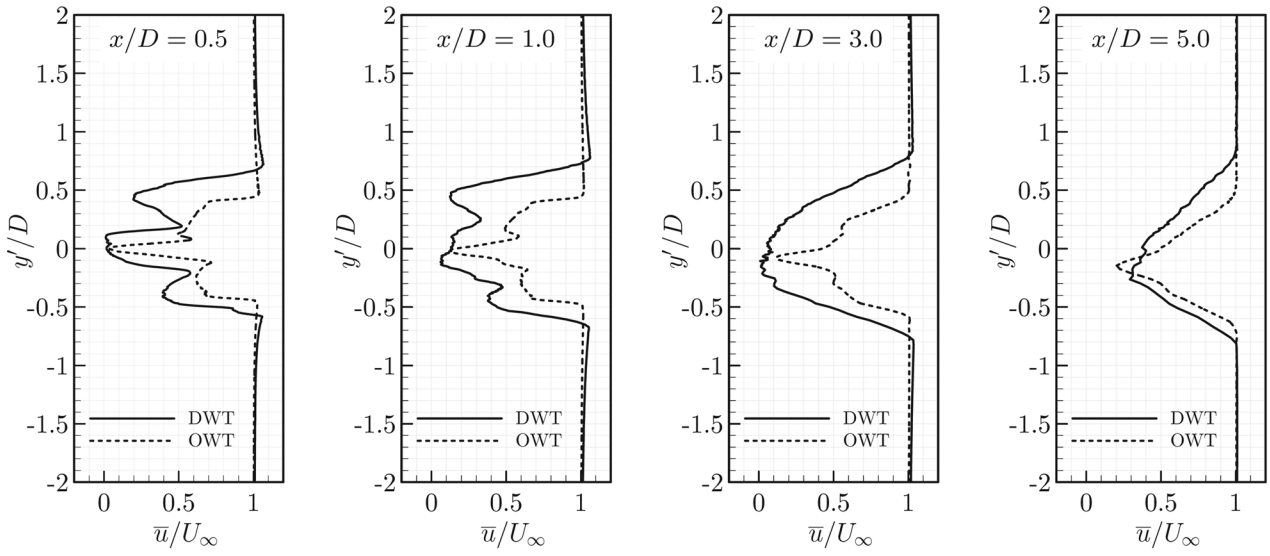

Fig. 20 Mean streamwise velocity profiles for $\gamma = 10$ deg

is just the opposite. The angle of attack decreases as the yaw angle increases, so no severe flow separation is observed in this region.

The mean streamwise velocity profiles at several locations in the central x'–y' plane are shown in Figs. 20–22 for the three nonzero yaw angles. To facilitate the discussion, we define the centerline of a wake as the line that connects points with minimum local streamwise flow speeds. This centerline divides a wake into an upper part and a lower part. From the profiles, it is seen that in the near field (e.g., $x'/D = 0.5$ and 1.0), the upper wakes overall travel slower than the lower wakes, indicating that the turbines may have extracted more energy via their upper parts. A comparison of the profiles further downstream, e.g., at $x'/D = 3.0$, reveals that the wakes of both turbines recover faster at larger yaw angles. Finally, the wake deflection is better judged from flows sufficiently downstream of the turbines, e.g., at $x'/D = 5.0$. For $\gamma = 10$ deg, the DWT's wake is slightly more deflected than the OWT's. For $\gamma = 20$ deg, the OWT's wake is slightly more deflected. For $\gamma = 30$ deg, the OWT's wake is obviously more deflected.

6 Summary

High-order implicit large eddy simulations of a ducted wind turbine and its open-rotor counterpart under different tip-speed ratios and different yaw angles have been successfully performed. The simulations employed a fifth-order spatial scheme, a third-order temporal scheme, and about 30×10^6 degrees-of-freedom. This is the first time that a high-order method being applied to a comprehensive study of a complete ducted wind turbine without any geometric simplification.

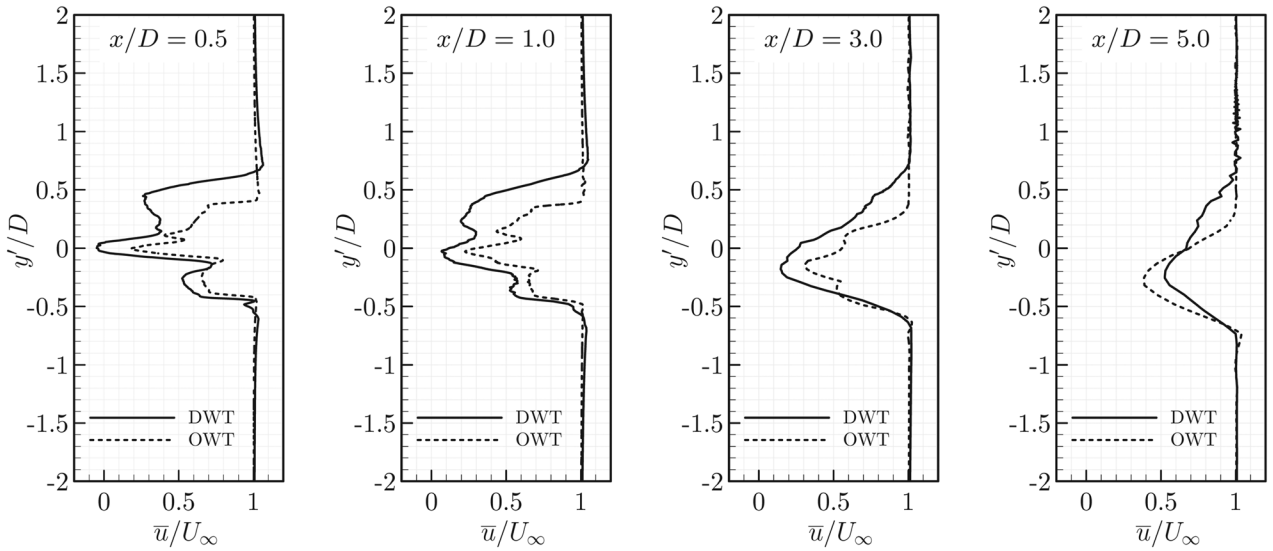

Fig. 21 Mean streamwise velocity profiles for $\gamma = 20$ deg

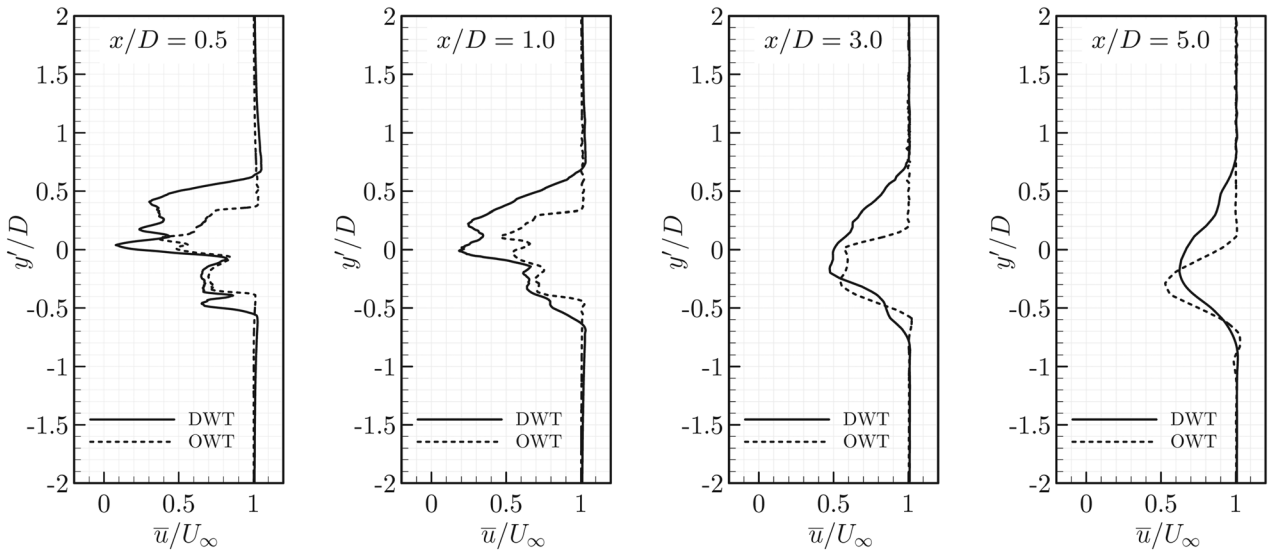

Fig. 22 Mean streamwise velocity profiles for $\gamma = 30$ deg

The simulation results reveal that the ducted turbine has much higher power outputs than its open-rotor counterpart for all the given tip-speed ratios. From pressure contours, it is identified that the loads concentrate more on the blades' outboard part, especially around the leading edges. From the isosurfaces of instantaneous Q-criterion, it is noticed that the presence of the duct has made the flow field more turbulent, weakened the tip and hub vortices, and enhanced the trailing edge vortices of the ducted turbine. As the tip-speed ratio increases, flow bifurcation is observed in the flow field of the ducted turbine. The contours and profiles of the mean streamwise velocity reveal that the bifurcation is caused by the increasing blockage effects of blade tips as the rotation speed increases.

Under yawed flow conditions, the ducted turbine is still found to have larger power outputs than the open configuration. It is confirmed that the ducted turbine's performance is insensitive to small yaw angles. Other than that, as the yaw angle increases, the thrust and the power coefficients both decrease, with the latter decreasing faster than the former. At nonzero yaw angles, the vortex fields are highly asymmetric for both turbines, and an interpretation using a disk analog and the angle of attack has been established. The velocity fields and profiles show that a large yaw angle may cause obvious flow deflections in the wakes, especially in the open turbine's wakes. Finally, the wake flows are found to recover more quickly at larger yaw angles.

Acknowledgment

The authors would like to express our acknowledgments to Clarkson University for financial support through the IGNITE Fellowship Program. C. Liang would also like to acknowledge support from the Office of Naval Research (No. N00014-20-1-2007) monitored by Dr. Ki-Han Kim. The computing hours (No. N00014-20-1-2007) were granted through the DoD HPC Modernization Program.

Conflict of Interests

There is no conflict of interest.

Data Availability Statement

The datasets generated and supporting the findings of this article are obtainable from the corresponding author upon reasonable request.

References

[1] Shepherd, W., and Zhang, L., 2017, *Electricity Generation Using Wind Power*, World Scientific, Singapore.
[2] Hau, E., 2013, *Wind Turbines: Fundamentals, Technologies, Application, Economics*, Springer Science & Business Media, Berlin, Germany.
[3] Burton, T., Jenkins, N., Sharpe, D., and Bossanyi, E., 2011, *Wind Energy Handbook*, Wiley, West Sussex, UK.
[4] Ochieng, F. X., Hancock, C. M., Roberts, G. W., and Le Kernec, J., 2018, "A Review of Ground-Based Radar as a Noncontact Sensor for Structural Health Monitoring of In-Field Wind Turbines Blades," Wind Energy, **21**(12), pp. 1435–1449.
[5] Dighe, V., Avallone, F., and Bussel, G., 2020, "Effects of Yawed Inflow on the Aerodynamic and Aeroacoustic Performance of Ducted Wind Turbines," J. Wind Eng. Ind. Aerodyn., **201**, p. 104174.
[6] Bontempo, R., and Manna, M., 2020, "On the Potential of the Ideal Diffuser Augmented Wind Turbine: An Investigation by Means of a Momentum Theory Approach and of a Free-Wake Ring-Vortex Actuator Disk Model," Energy Convers. Manage., **213**, p. 112794.
[7] Lilley, G. M., and Rainbird, W. J., 1956, *A Preliminary Report on the Design and Performance of Ducted Windmills*, College of Aeronautics, Cranfield University, Bedford, UK.
[8] Foreman, K. M., Gilbert, B., and Oman, R. A., 1978, "Diffuser Augmentation of Wind Turbines," Sol. Energy, **20**(4), pp. 305–311.
[9] Gilbert, B. L., and Foreman, K. M., 1979, "Experimental Demonstration of the Diffuser-Augmented Wind Turbine Concept," J. Energy, **3**(4), pp. 235–240.
[10] Igra, O., 1981, "Research and Development for Shrouded Wind Turbines," Energy Convers. Manage., **21**(1), pp. 13–48.
[11] Fletcher, C. A., 1981, "Computational Analysis of Diffuser-Augmented Wind Turbines," Energy Convers. Manage., **21**(3), pp. 175–183.
[12] Vaz, J. R., and Wood, D. H., 2018, "Effect of the Diffuser Efficiency on Wind Turbine Performance," Renewable Energy, **126**, pp. 969–977.
[13] Koras, A. D., and Georgalas, C. G., 1988, "Calculation of the Influence of Annular Augmentors on the Performance of a Wind Rotor," Wind Eng., **12**(4), pp. 257–267.
[14] Politis, G. K., and Koras, A. D., 1995, "A Performance Prediction Method for Ducted Medium Loaded Horizontal Axis Windturbines," Wind Eng., **19**(5), pp. 273–288.
[15] Phillips, D. G., Richards, P. J., and Flay, R., 2002, "CFD Modelling and the Development of the Diffuser Augmented Wind Turbine," Wind Struct., **5**(2_3_4), pp. 267–276.
[16] Hansen, M. O. L., Sørensen, N. N., and Flay, R. G. J., 2000, "Effect of Placing a Diffuser Around a Wind Turbine," Wind Energy, **3**(4), pp. 207–213.
[17] Abe, K., and Ohya, Y., 2004, "An Investigation of Flow Fields Around Flanged Diffusers Using CFD," J. Wind Eng. Ind. Aerodyn., **92**(3–4), pp. 315–330.
[18] Venters, R., Helenbrook, B., and Visser, K., 2018, "Ducted Wind Turbine Optimization," ASME J. Sol. Energy Eng., **140**(1), p. 011005.
[19] Sadeghi, N. B., Helenbrook, B., and Visser, K., 2018, "Ducted Wind Turbine Optimization and Sensitivity to Rotor Position," Wind Energy Sci., **3**(1), pp. 221–229.
[20] Hill, W. R. T., 1973, "Triangular Mesh Methods for the Neutron Transport Equation," Los Alamos Scientific Laboratory, Los Alamos, NM, Technical Report No. LA-UR-73-479; CONF-730414-2.
[21] Cockburn, B., Karniadakis, G., and Shu, C. W., 2012, *Discontinuous Galerkin Methods: Theory, Computation and Applications*, Vol. 11, Springer Science & Business Media, Berlin, Germany.
[22] Patera, A., 1984, "A Spectral Element Method for Fluid Dynamics: Laminar Flow in a Channel Expansion," J. Comput. Phys., **54**(3), pp. 468–488.
[23] Karniadakis, G., and Sherwin, S., 2013, *Spectral/hp Element Methods for Computational Fluid Dynamics*, Oxford University Press, Oxford, UK.
[24] Kopriva, D., and Kolias, J., 1996, "A Conservative Staggered-Grid Chebyshev Multidomain Method for Compressible Flows," J. Comput. Phys., **125**(1), pp. 244–261.
[25] Kopriva, D., 1996, "A Conservative Staggered-Grid Chebyshev Multidomain Method for Compressible Flows. II. A Semi-Structured Method," J. Comput. Phys., **128**(2), pp. 475–488.
[26] Kopriva, D., 1998, "A Staggered-Grid Multidomain Spectral Method for the Compressible Navier–Stokes Equations," J. Comput. Phys., **143**(1), pp. 125–158.
[27] Liu, Y., Vinokur, M., and Wang, Z., 2006, "Spectral Difference Method for Unstructured Grids I: Basic Formulation," J. Comput. Phys., **216**(2), pp. 780–801.
[28] Huynh, H. T., 2007, "A Flux Reconstruction Approach to High-Order Schemes Including Discontinuous Galerkin Methods," AIAA Paper No. 2007-4079.
[29] Huynh, H. T., 2009, "A Reconstruction Approach to High-Order Schemes Including Discontinuous Galerkin for Diffusion," AIAA Paper No. 2009-403.
[30] Wang, Z. J., and Gao, H., 2009, "A Unifying Lifting Collocation Penalty Formulation Including the Discontinuous Galerkin, Spectral Volume/Difference Methods for Conservation Laws on Mixed Grids," J. Comput. Phys., **228**(21), pp. 8161–8186.
[31] Zhang, B., and Liang, C., 2015, "A Simple, Efficient, High-Order Accurate Sliding-Mesh Interface Approach to FR/CPR Method on Coupled Rotating and Stationary Domains," AIAA Paper No. 2015-1742.
[32] Zhang, B., and Liang, C., 2015, "A Simple, Efficient, and High-Order Accurate Curved Sliding-Mesh Interface Approach to Spectral Difference Method on Coupled Rotating and Stationary Domains," J. Comput. Phys., **295**, pp. 147–160.
[33] Zhang, B., Liang, C., Yang, J., and Rong, Y., 2016, "A 2D Parallel High-Order Sliding and Deforming Spectral Difference Method," Comput. Fluids, **139**, pp. 184–196.
[34] Zhang, B., and Liang, C., 2016, "A High-Order Sliding-Mesh Spectral Difference Solver for Simulating Unsteady Flows Around Rotating Objects," 31st Symposium on Naval Hydrodynamics, Monterey, CA, Sept. 11–16, pp. 1–15.
[35] Zhang, B., Qiu, Z., and Liang, C., 2018, "A Flux Reconstruction Method With Nonuniform Sliding-Mesh Interfaces for Simulating Rotating Flows," AIAA Paper No. 2018-1094.
[36] Zhang, B., and Liang, C., 2021, "A Conservative High-Order Method Utilizing Dynamic Transfinite Mortar Elements for Flow Simulation on Curved Sliding Meshes," J. Comput. Phys., **443**, p. 110522.
[37] Zhang, B., and Liang, C., 2019, "High-Order Numerical Simulation of Flows Over Rotating Cylinders of Various Cross-Sectional Shapes," AIAA Paper No. 2019-3430.
[38] Zhang, B., and Liang, C., 2019, "High-Order Numerical Simulation of Flapping Wing for Energy Harvesting," AIAA Paper No. 2019-3338.
[39] Zhang, B., Ding, C., and Liang, C., 2021, "High-Order Implicit Large-Eddy Simulation of Flow Over a Marine Propeller," Comput. Fluids, **224**, p. 104967.
[40] Ding, C., Zhang, B., Liang, C., Visser, K. D., and Yao, G., 2022, "High-Order Large-Eddy Simulations of a Ducted Wind Turbine," AIAA Paper No. 2022-1147.
[41] Thomas, P. D., and Lombard, C. K., 1979, "Geometric Conservation Law and Its Application to Flow Computations on Moving Grids," AIAA J., **17**(10), pp. 1030–1037.
[42] Ergatoudis, I., Irons, B. M., and Zienkiewicz, O. C., 1968, "Curved, Isoparametric, 'Quadrilateral' Elements for Finite Element Analysis," Int. J. Solids Struct., **4**(1), pp. 31–42.
[43] Rusanov, V. V., 1961, "Calculation of Interaction of Non-Steady Shock Waves With Obstacles," J. Comput. Math. Phys. USSR, **1**, pp. 267–279.
[44] Spiteri, R. J., and Ruuth, S. J., 2002, "A New Class of Optimal High-Order Strong-Stability-Preserving Time Discretization Methods," SIAM J. Numer. Anal., **40**(2), pp. 469–491.
[45] Ruuth, S., 2005, "Global Optimization of Explicit Strong-Stability-Preserving Runge–Kutta Methods," Math. Computation, **75**(253), pp. 183–207.
[46] Zhang, B., 2016, "A High-Order Computational Framework for Simulating Flows Around Rotating and Moving Objects," Ph.D. thesis, The George Washington University, Washington, DC.
[47] Kanya, B., and Visser, K., 2018, "Experimental Validation of a Ducted Wind Turbine Design Strategy," Wind Energy Sci., **3**(2), pp. 919–928.